UV light emitting transparent conducting tin-doped indium oxide (ITO) nanowires

2011 Nanotechnology 22 195706

(http://iopscience.iop.org/0957-4484/22/19/195706)

Nanotechnology **22** (2011) 195706 (10pp) doi:10.1088/0957-4484/22/19/195706

UV light emitting transparent conducting tin-doped indium oxide (ITO) nanowires

J Gao[1], R Chen[1], D H Li[1], L Jiang[2], J C Ye[3], X C Ma[3], X D Chen[2], Q H Xiong[1], H D Sun[1] and T Wu[1,4]

[1] Division of Physics and Applied Physics, School of Physical and Mathematical Sciences, Nanyang Technological University, Singapore 637371, Singapore
[2] School of Materials Science and Engineering, Nanyang Technological University, Singapore 639798, Singapore
[3] College of Materials Science and Engineering, Shenzhen University, Shenzhen, Guangdong, 518060, People's Republic of China

E-mail: Tomwu@ntu.edu.sg

Received 5 December 2010, in final form 24 February 2011
Published 23 March 2011
Online at stacks.iop.org/Nano/22/195706

Abstract
Multifunctional single crystalline tin-doped indium oxide (ITO) nanowires with tuned Sn doping levels are synthesized via a vapor transport method. The Sn concentration in the nanowires can reach 6.4 at.% at a synthesis temperature of 840 °C, significantly exceeding the Sn solubility in ITO bulks grown at comparable temperatures, which we attribute to the unique feature of the vapor–liquid–solid growth. As a promising transparent conducting oxide nanomaterial, layers of these ITO nanowires exhibit a sheet resistance as low as 6.4 Ω/□ and measurements on individual nanowires give a resistivity of 2.4×10^{-4} Ω cm with an electron density up to 2.6×10^{20} cm^{-3}, while the optical transmittance in the visible regime can reach ∼80%. Under the ultraviolet excitation the ITO nanowire samples emit blue light, which can be ascribed to transitions related to defect levels. Furthermore, a room temperature ultraviolet light emission is observed in these ITO nanowires for the first time, and the exciton-related radiative process is identified by using temperature-dependent photoluminescence measurements.

S Online supplementary data available from stacks.iop.org/Nano/22/195706/mmedia

(Some figures in this article are in colour only in the electronic version)

1. Introduction

The synthesis of multifunctional nanomaterials is a ubiquitous theme in nanoscience aimed at integrating multiple functionalities into individual building blocks to enable the fabrication of novel devices. The central challenge is to realize multiple functionalities synergistically in individual materials. Transparent conducting oxides (TCO) combining high transparency and superb conductivity are widely used in various technologically important applications such as solar cells [1–3], flat panel displays [4], and antireflective coatings [5]. As a prominent TCO, tin-doped indium oxide (ITO) thin films have been intensively investigated owing to their excellent electrical conductivity and optical transparency. In various emerging technologies, one-dimensional nanostructures like nanowires possess great potential due to their unique properties associated with high aspect ratio and good crystallinity [6]. Catering to the needs in flexible electronics [7–9], several groups have proposed replacing ITO thin films with meshes of nanoscale building blocks like carbon nanotubes and silver nanowires [10, 11]. Although these alternatives compare favorably to ITO thin films in terms of flexibility, it is more advantageous to use ITO nanowires which give the intrinsic merits of being transparent and conducting. Indeed, by using thin layers of ITO nanowires as transparent top contacts, optimum electronic and photonic performances were recently demonstrated in light emitting devices [12]. There have also been reports on the successful synthesis of ITO nanostructures with good performance via physical vapor transportation methods [4, 13, 14], These nanowires are promising in a wide range of applications in nanoscale electronic and optoelectronic devices. However, there is an

[4] Author to whom any correspondence should be addressed.

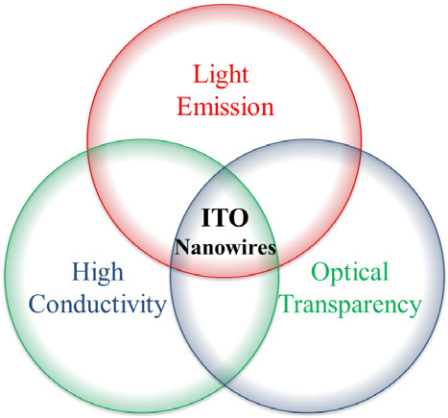

Figure 1. Illustration of ITO nanowires integrating three important functionalities: UV light emission, high conductivity, and optical transparency.

urgent need to achieve a rational control on the Sn doping in ITO nanowires which critically determines their conductivity and transparency. Furthermore, the optical characteristics, in particular the excitonic radiative process, in ITO nanowires have not been reported.

In this work, we report on the vapor transport synthesis of multifunctional ITO nanowire layers which show excellent electrical and optical properties as a TCO material. Importantly, under similar thermodynamic conditions these ITO nanowires demonstrated a better tin doping tunability than that of the bulk counterpart. Furthermore, we carried out photoluminescence (PL) measurements on these ITO nanowires, and observed for the first time an ultraviolet (UV) emission at room temperature. Temperature-dependent PL measurements were employed to reveal the mechanism of the exciton-related radiation. As illustrated in figure 1, our results achieved on the ITO nanowires with tunable compositions help to establish a novel multifunctional material combining the merits of light emission, being transparent and conductive. These light emitting TCO nanowires may find widespread applications in functional integrated devices.

2. Experimental work

The single crystalline ITO nanowires were synthesized by using a vapor transport method as described in detail in previous reports [15–19]. A mixture of In_2O_3, SnO_2 (Sigma-Aldrich, purity 99.99%), and graphite fine powders was loaded into a horizontal tube furnace equipped with a pumping and gas regulating system. The graphite powder here acts as the reduction agent to release metal vapors. Ultrasonically cleaned Si (111) or quartz or α-cut sapphire substrates with sputtered Au thin layers (1–3 nm) as catalyst were positioned 3–7 cm downstream from the source. A stream of argon gas (Ar, purity 99.995%) with a flow rate of 100 sccm (standard cubic centimeter) was introduced as the carrier gas, and a growth pressure of 30 mbar was maintained in the tube furnace. After staying at 200 °C for 20 min to dry the source powder, the furnace temperature was elevated to the growth temperature of 840 °C at a rate of 40 °C min^{-1}, then cooled down naturally to room temperature within half an hour after growth. In control experiments, ITO powder samples were synthesized by using the standard solid state reaction method. In_2O_3 and SnO_2 fine powders (Sigma-Aldrich, purity 99.99%) were thoroughly mixed before being dried and pressed uniaxially into pellets which were then sintered at 1350 °C in air for 10 h. In the fabrication of nanowire devices, ITO nanowires were firstly dispersed into acetone solutions and then deposited onto silicon substrates with a 200 nm silicon dioxide layer. Electrodes were defined by using an e-beam lithography process and Cr/Au(10 nm/150 nm) deposition/lift-off.

The morphology and structure of ITO nanowires were characterized by using a field-emission scanning electron microscope (FESEM) (JEOL, JSM-6700F-FESEM), an x-ray diffractometer (XRD) (Bruker D8 Advanced diffractometer and Rigaku SmartLab), and a high-resolution transmission electron microscope (HRTEM) (JEOL, 2100). Energy dispersive x-ray spectroscopy (EDS) and x-ray photoelectron spectroscopy (XPS) (VG ESCALAB 200i-XL) were employed for elemental analysis. Sheet resistance and temperature-dependent resistance measurements were performed on ITO nanowire layers with the van der Pauw configuration [20] using a room temperature probe station (SUSS MicroTec) and a cryogen free refrigerator system (JANIS, CCS-100/202). Hall effect measurements were carried out in a cryogenic probe station (JANIS ST500). Optical transmittance measurements were performed in a UV–visible–near infrared (UV–vis–NIR) double beam spectrophotometer (Perkin Elmer Lambda 950) in ambient. Temperature-dependent PL measurements were carried out using a He–Cd laser (325 nm) as the excitation source.

3. Results and discussion

3.1. Synthesis and characterizations of ITO nanowires with tuned Sn concentrations

After systematically exploring the effects of various growth parameters, we found that by carefully adjusting the source powder composition ($In_2O_3/SnO_2/C$), tin doping can be effectively tuned. A typical series of experiments consists of eight samples sequentially prepared by varying the tin concentration in the source while keeping the other growth conditions unchanged (table 1); samples labeled from IO to ITO-7 correspond to the eight different SnO_2 weight concentrations in the source ranging from 0 to 60%. The SEM image in figure 2(a) (sample ITO-5) shows a layer of long, straight, and randomly oriented nanowires on the silicon substrate after growth of 1 h. Closer examinations (see figure 2(b)) revealed the square-shaped cross-section of the nanowires with a pyramid tip. The nanoparticles on the top indicate the dominant vapor–liquid–solid (VLS) growth mechanism [21, 22], Furthermore, the mismatch between the nanoparticle and nanowire dimensions implies the possible involvement of the vapor–solid (VS) growth [23]. As we increased the tin concentration, the morphology of the nanowire did not change much initially, then at the highest tin

Table 1. Correlation between the source compositions and the resulting Sn doping concentrations in ITO nanowires. All the growth conditions for the vapor transport growth except the source composition were kept the same. The lattice constants and the Sn concentrations were calculated from the XRD and the EDS data.

Sample no.	Source composition (wt ratio)	Tin atomic% in source powder (at.%)	Lattice constant of nanowires (Å)	Tin atomic% in nanowires (at.%)
IO	In_2O_3:C = 1.0:1.0	0	10.117(7)	0
ITO-1	SnO_2:In_2O_3:C = 0.05:0.95:1.0	4.6	10.120(5)	1.0 ± 0.1
ITO-2	SnO_2:In_2O_3:C = 0.1:0.9:1.0	9.3	10.123(1)	2.0 ± 0.1
ITO-3	SnO_2:In_2O_3:C = 0.2:0.8:1.0	19	10.125(1)	3.9 ± 0.2
ITO-4	SnO_2:In_2O_3:C = 0.3:0.7:1.0	28	10.124(4)	3.8 ± 0.6
ITO-5	SnO_2:In_2O_3:C = 0.4:0.6:1.0	38	10.127(6)	5.1 ± 0.5
ITO-6	SnO_2:In_2O_3:C = 0.5:0.5:1.0	48	10.131(1)	6.4 ± 0.3
ITO-7	SnO_2:In_2O_3:C = 0.6:0.4:1.0	58	10.131(5)	—

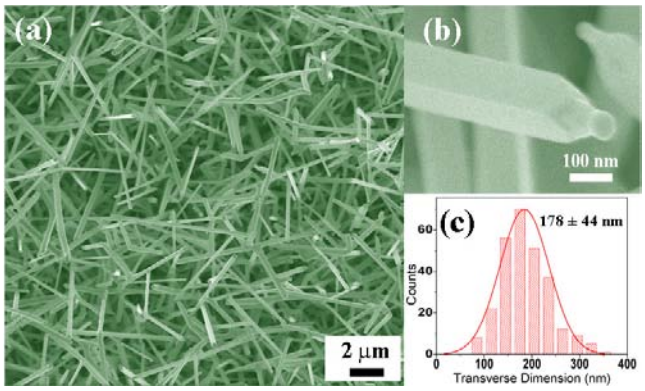

Figure 2. (a) SEM top view of ITO nanowires grown on silicon substrate (sample ITO-5); (b) enlarged view of a nanowire; (c) corresponding histogram of the transverse dimensions of ITO nanowires.

ratios triangular nanosheets appeared as a result of enhanced side growth (supporting information: figure S1 available at stacks.iop.org/Nano/22/195706/mmedia). Typically the nanowires have an average dimension of ∼180 nm (see figure 2(c)) and length of a few micrometer.

It is well recognized that doping nanowires in the vapor transport growth is quite challenging; the doping concentration in the growth products could be well below that in the source powder. To investigate the reliability and efficiency of our doping strategy based on the vapor transport method, we carried out extensive XRD studies on several series of ITO nanowire samples. The XRD patterns of the eight ITO nanowire samples listed in table 1 are given in figure 3(a). Their phase was identified to be the In_2O_3 cubic bixbyite structure (JCPDS #17-2195). Precipitation of SnO_2 in the In_2O_3 matrix emerges when the SnO_2 weight percentage in the source powder reaches over 50%, as indicated by the emergence of the SnO_2 rutile phase in the XRD pattern, which suggests that the doping limit is reached. The shift of the (440) peak to smaller angles (see figure 3(b)) confirms the Sn doping in the nanowires [24], but contradicts Vegard's Law which predicts a contraction in lattice constant due to the smaller radius of the Sn^{4+} ion (0.71 Å) compared with that of the In^{3+} ion (0.81 Å); this contradiction can be attributed to the large repulsive force arising from the additional positive charges of the Sn cations [25, 24] or the increase of interstitial O which neutralizes the extra positive charges [26]. In figure 3(c), the lattice constants of the ITO nanowire samples were calculated from the XRD data and plotted as a function of the molar ratio of SnO_2 in the source (red circles). The lattice constant reaches a maximum value as the SnO_2 weight concentration increases to 50%, implying that the Sn content saturates in the In_2O_3 matrix. This maximum in solubility coincides with the emergence of the SnO_2 phase, as shown in figure 3(a).

In order to quantitatively determine the Sn concentration in the samples, ITO powder samples with different doping levels were synthesized as reference samples by using the solid state reaction. In_2O_3 and SnO_2 powders with appropriate ratios were thoroughly mixed and then pressed into pellets, which were then sintered at 1350 °C in air for 10 h. Such a high sintering temperature was chosen because of the low SnO_2 solubility in In_2O_3 at lower temperatures. To ensure uniformity of the powder samples, the mixing and sintering process was repeated three times. Six ITO powder samples with different Sn concentrations were prepared, and the XRD studies did not show any SnO_2 rutile phase when the Sn concentration was below 4 at.% (supporting information: figure S3 available at stacks.iop.org/Nano/22/195706/mmedia). To compare this with the nanowire samples, the lattice constant of these powder samples was calculated based on the position of the (440) peak. The plot of lattice constant versus Sn concentration (see figure 3(c), blue triangles) shows that the lattice constant increases with the Sn concentration and eventually saturates at around 10.125 Å. These results indicate that the Sn concentration in ITO powder samples cannot exceed 4 at.% at the processing temperature of 1350 °C. We should note here that many previous works have reported on the solid state solubility of SnO_2 in both bulk and thin film In_2O_3, but there are large discrepancies, which sometimes are ascribed to different measurement techniques [26–29]. The solubility reported here is in agreement with the previously reported values, e.g. 5 at.% at temperatures below 1450 °C by Nadaud *et al* [28] and Udawatte and Yanagisawa [29], and 4 at.% at 1350 °C by Heward *et al* [30]. These reports also documented similar behavior of lattice constants with respect to the Sn concentration. The comparison of the lattice constants of the ITO powder samples with the nanowire samples in figure 3(c) helped to determine the tin concentrations in the first three nanowire samples with the lowest Sn doping (1.0, 2.0, and

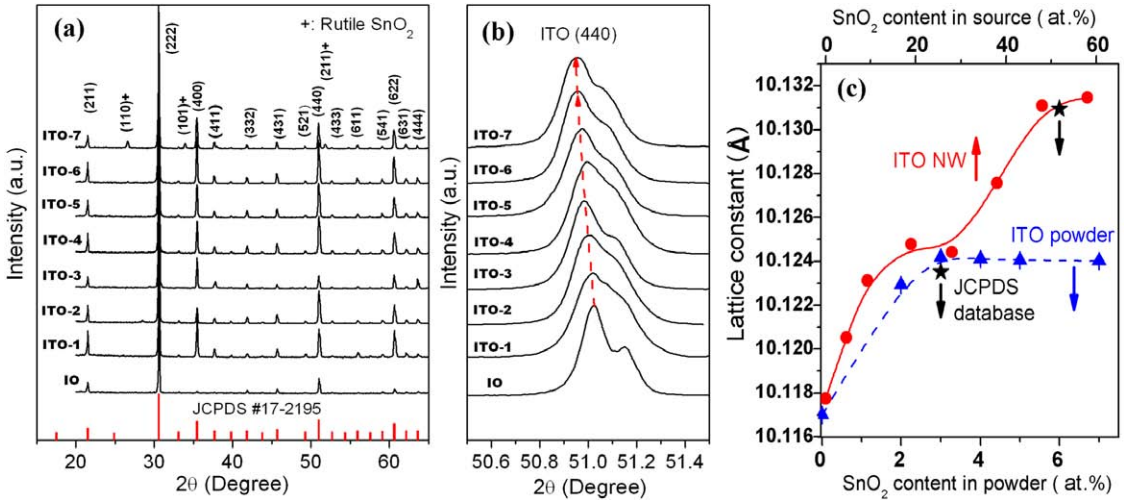

Figure 3. (a) XRD patterns of the ITO nanowires grown on silicon substrates. (b) Fine scans of the ITO (440) peak, with the dashed line tracking the peak position. The shoulders at higher angle are due to the unfiltered K α_2 component from the x-ray source (supporting information available at stacks.iop.org/Nano/22/195706/mmedia). (c) Dependence of the lattice constant on the source composition for the ITO nanowire samples (red circles) and the ITO powder samples (blue triangles). The lines are guides to the eyes. As reference, the lattice constants from the JCPDS database at two Sn concentrations of 3 at.% and 6 at.% are also shown as black stars.

3.9 at.%, respectively, table 1). However, for the rest of the samples, as the lattice constants of the nanowire samples are larger than those of the ITO powders, other analysis tools were used to determine the tin concentration, as we will discuss later.

Structural characterizations on ITO nanowires were performed by using a TEM. A bright field TEM image of an ITO nanowire from sample ITO-6 with a transverse dimension of ∼100 nm is given in figure 4(a). The corresponding HRTEM image and the selected area electron diffraction (SAED) pattern are shown in figures 4(b) and (c), respectively. The HRTEM image indicates the high crystalline nature of the nanowires, and the Sn doping did not cause any obvious dislocation or cluster formation (supporting information available at stacks.iop.org/Nano/22/195706/mmedia). The SAED pattern confirms the cubic bixbyite structure of the ITO nanowires. The two inter-plane distances were measured, and the lattice planes can be indexed to ITO (200) and (011) as shown in figure 4(b). The growth direction was identified to be [100], consistent with the previous reports [12, 31].

EDS was performed to further determine the doping level. We surveyed several samples, and the results from the first few samples are consistent with those derived from the XRD data by comparison with the powder samples. The EDS spectrum taken on sample ITO-6 is given in figure 4(d), from which the Sn concentration was determined to be 6.4 at.%, in agreement with the JCPDS database (figure 3(c) black stars). The Cu and C signals come from the copper grid and carbon lacey film on the grid. Based on the EDS data, also taking into account the XRD results, we determined the Sn concentrations in samples ITO-1 to ITO-6 to be 1.0, 2.0, 3.9, 3.8, 5.1, and 6.4 at.%, respectively (see table 1). Moreover, the EDS mappings along the nanowire (see figure 4(e)) revealed uniform elemental distributions. In addition, XPS was carried out to confirm the composition of nanowires and to determine the valence state of Sn ions. A typical survey spectrum taken on sample ITO-6 was given in figure 4(f). The Sn ($3d_{5/2}$) peak was fitted with a single component centered at 487.5 eV with a full width at half maximum (FWHM) of 1.59 eV, corresponding to a valence state of Sn^{4+} [32].

Doping Sn into In_2O_3 is challenging due to several obstacles. First, the tetragonal SnO_2 has little affinity for the bixbyite In_2O_3, which is reflected by the high entropy (11.8 J mol^{-1} K^{-1}) and enthalpy (60 980 J mol^{-1}) associated with the solid state reaction. Second, the large atomic radius difference (13.75%) between Sn^{4+} and In^{3+} hampers the Sn doping into In_2O_3 [30, 31]. Finally, the formation energy of defects caused by doping in nanocrystals is much larger than that in bulk due to the 'self-purification' mechanism [33, 34], which often makes doping nanomaterials a formidable task. Surprisingly, as shown in figure 3(c), comparing the Sn doping levels in the powder and the nanowire samples revealed that the doping concentration in ITO nanowires deposited at a synthesis temperature of 840 °C can be much higher than that of the bulk counterparts processed at 1350 °C. The enhanced solubility in the ITO nanowires can be ascribed to the unique aspects of VLS growth. In this catalyzed synthesis, Au catalyst nanoparticles absorb Sn and In, and the heterogeneous precipitation at supersaturation leads to the growth of ITO nanowires. During the dynamic growth which often occurs under non-equilibrium conditions, the liquid-state alloy nanoparticles may sustain a large Sn/In ratio [35], which eventually leads to the high Sn concentration in ITO nanowires (supporting information: figure S5, available at stacks.iop.org/Nano/22/195706/mmedia). Similar results were observed in the synthesis of ITO thin film, in which thermodynamically metastable Sn-doped In_2O_3 with a Sn concentration well exceeding the bulk solubility limit was achieved under non-equilibrium synthesis conditions [36, 37]. In contrast, the solid state reaction method used in the synthesis of ITO powder samples relies on the mutual inter-diffusion between SnO_2 and

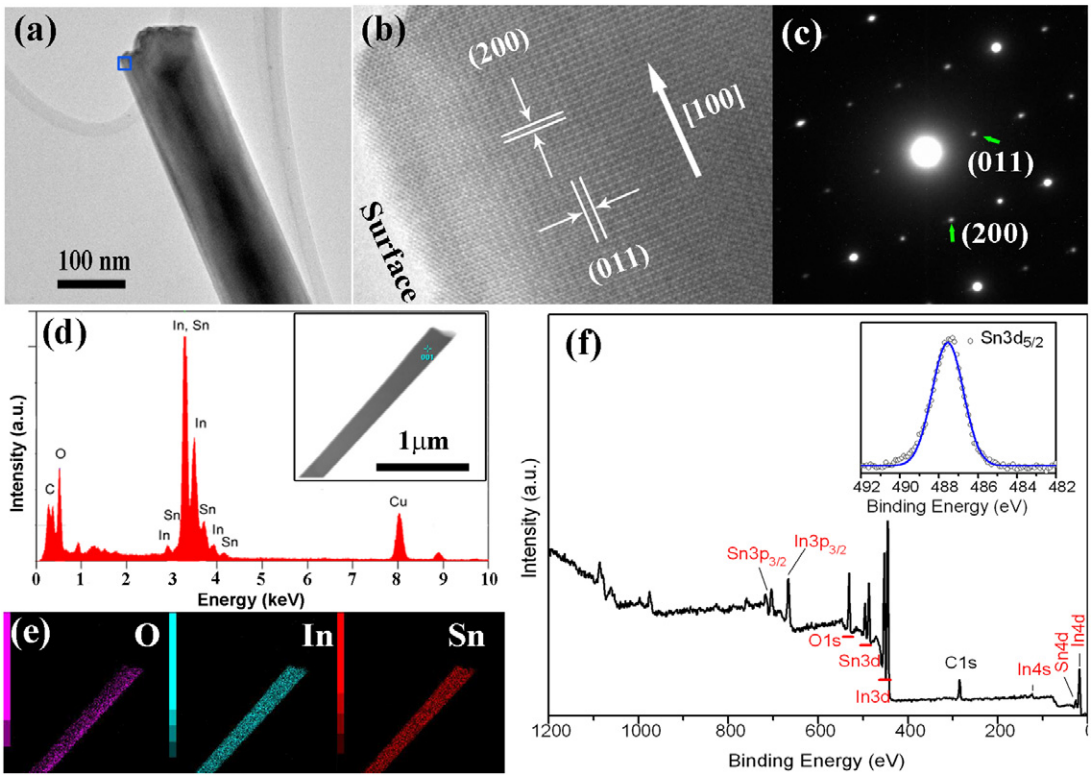

Figure 4. (a) Bright field TEM image of an ITO nanowire from sample ITO-6; (b) HRTEM image of the selected area in (a) showing the good crystallinity and the growth direction along [100]; (c) corresponding SAED pattern; (d) EDS spectrum taken on an ITO nanowire (ITO-6) shown in the inset; (e) corresponding elemental mappings; (f) XPS survey spectrum of sample ITO-6. Insets show the fine scan of the Sn $3d_{5/2}$ peak. Circles and the blue line are the data and the fitting result, respectively.

In_2O_3 granular powder, where high temperatures are needed to overcome the activation barrier for thermal diffusion. This slow atomic diffusion in solid state reactions also involves a high thermal budget, i.e. high temperature sintering for several hours or more. Therefore, we can ascribe the significantly improved Sn solubility in ITO nanowires compared with powder samples to the distinct synthesis route.

3.2. Electrical properties of ITO nanowires

The electrical properties of thin layers of ITO nanowires with different Sn doping levels were characterized by using the van der Pauw configuration [20]. These nanowire layers were directly synthesized on Si substrates, and their thickness was controlled by adjusting the growth time (supporting information: figure S7 available at stacks.iop.org/Nano/22/195706/mmedia). As shown in figure 5(a) (red squares), the sheet resistance of ITO nanowire layers decreases from 11.71 to 6.35 Ω/□ with increasing Sn doping. This is remarkable considering that the nanowires in the layers are not well connected, and the electron conduction depends on the percolative current flow in the random nanowire network (inset of figure 5(a)). Unlike the polycrystalline thin films [38], one important merit of these single-crystal nanowires is their high crystalline quality, which makes them free from grain boundary scattering and improves the conductivity.

To eliminate the effect of network configuration in nanowire layers, we also carried out transport measurements on individual ITO nanowires. After nanowires were dispersed on Si substrates with 200 nm silicon dioxide insulating layers, electrodes of Cr/Au (10 nm/150 nm) were defined by using electron beam lithography. Figure 5(b) shows a typical I–V curve obtained by using the four-probe configuration (see inset of figure 5(b)) on a nanowire from the sample ITO-6 which has the highest tin doping level. We also note here that the ohmic contact between the Cr/Au electrodes and the ITO nanowires was readily achieved as indicated by the linear I–V curves between any two probes. Conductivity of the individual ITO nanowires was calculated based on their dimensions, and a typical value of 2.4×10^{-4} Ω cm was achieved, which is comparable to that of ITO thin films [39]. Such a good conductivity of ITO nanowires makes them very promising for applications as interconnects in optoelectronic nanodevices.

Moreover, the Hall measurements carried out on nanowire layers show that the mobility decreases from 11.93 to 2.21 $cm^2\ V^{-1}\ s^{-1}$ as the Sn doping increases (see figure 5(a), blue circles), which is in good agreement with the previous studies on ITO thin films [40, 41]; Sn doping lowers the mobility by enhancing the phonon and ionized impurity related scattering [42–44]. Figure 5(c) shows the temperature dependence of resistance (R–T) measured in the sample ITO-1 which has the lowest Sn doping level of 1.0 at.%. Within the whole temperature range from 14 to 300 K, a metallic transport behavior was observed.

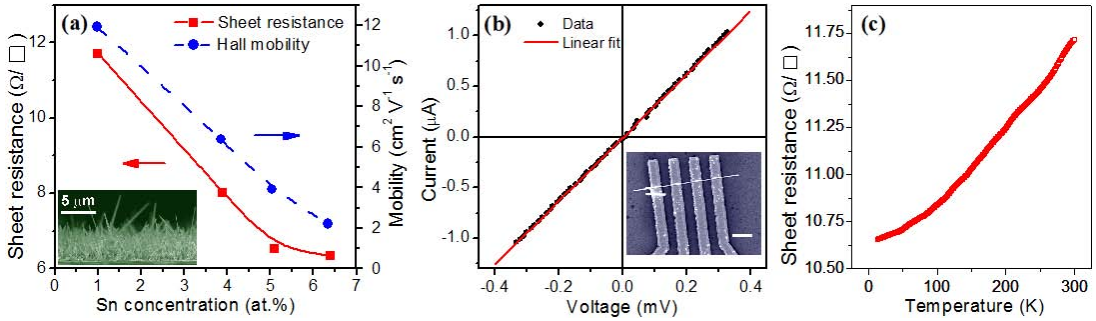

Figure 5. (a) Room temperature sheet resistance (red squares) and Hall mobility (blue circles) versus Sn doping level in ITO nanowires. Inset is the cross-sectional SEM image of the ITO nanowire layer. (b) Room temperature current versus voltage curve measured on an individual nanowire from the sample ITO-6 with the highest tin doping level. A linear fit is also shown. Inset is the SEM image of the nanowire device made using electron beam lithography. The scale bar represents 1 μm. (c) R–T characteristic of sample ITO-1 with the lowest Sn doping level (1.0 at.%) showing a metallic transport behavior.

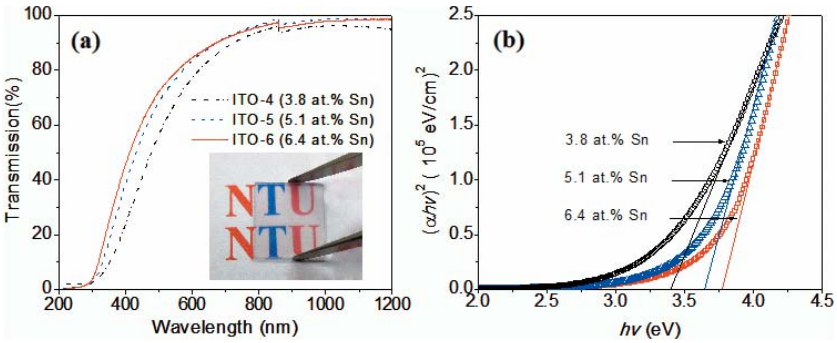

Figure 6. (a) Transmittance spectra of ITO nanowire layers grown on quartz substrates. The inset shows the photograph of the 1 cm^2 sample. The kinks at 860 nm are due to the detector switching. (b) Corresponding plot of $(\alpha h\upsilon)^2$ versus $h\upsilon$. The intercepts of linear extrapolations give the optical band gaps.

3.3. Optical properties of ITO nanowires

As a versatile TCO nanomaterial, the optical property of ITO nanowires has not been systematically investigated so far. To probe the optical transmittance properties, thin layers of ITO nanowires were grown on quartz substrates; structural and elemental analyses revealed very similar characteristics in the samples grown on quartz and silicon substrates. Transmittance measurements were performed on the ITO nanowire samples with a UV–vis–NIR double beam spectrophotometer. Figure 6(a) shows the transmittance spectra for the samples ITO-4, ITO-5, and ITO-6 with Sn doping levels of 3.8, 5.1, and 6.4 at.%, respectively. An average transmittance of 80% in the visible range was observed in all samples, and it increases to 95% at the NIR wavelengths. Unlike thin films, there is no Fabry–Pérot interference in ITO nanowires due to the absence of a flat top surface. The lower transmittance at the shorter wavelength can be ascribed to the scattering effect from the randomly oriented nanowires [45]. The size of nanowires (100–200 nm) and the ITO refractive index of 2.19 suggest a scattering enhancement in the wavelength range of 220–440 nm, which is in line with the transmittance data.

Moreover, a blue shift in the absorption edge with the increasing doping concentration was also observed in figure 6(a). Figure 6(b) depicts the plots of $(\alpha h\upsilon)^2$ versus $h\upsilon$ for the same set of samples with α, d, h, and υ being the absorption coefficient, the layer thickness, the Planck constant, and the frequency, respectively. The onset of strong absorption corresponds to the optical band gap (E_g^{op}), which can be ascribed to the transition from the conduction band minimum (CBM) to an energy level below the valence band maximum (VBM), while the direct CBM–VBM transition is parity forbidden [46]. The optical band gap can be determined using the Tauc's relationship [47, 48]:

$$\alpha h\upsilon \propto (h\upsilon - E_g^{op})^{1/2}. \quad (1)$$

E_g^{op} of the three ITO nanowire samples were found to be 3.4 ± 0.1, 3.7 ± 0.1, and 3.8 ± 0.1 eV, respectively, which systematically increases with the Sn doping. According to the Burstein–Moss model [49, 50], this band gap increase is due to the filling up of low energy states in the conduction band by the doped electrons. Since the optical band gap for the undoped In_2O_3 is 3.3 ± 0.1 eV [51], the Burstein–Moss shifts in ITO-4, ITO-5, and ITO-6 can be estimated to be 0.1, 0.4, and 0.5 eV, respectively. This Burstein–Moss shift ΔE^{BM} is directly related to the electron concentration (n):

$$\Delta E^{BM} = (h^2/8\pi^2 m^*)(3\pi^2 n)^{2/3}, \quad (2)$$

where m^* is the electron effective mass. Given $m^* = 0.3m_e$, the carrier concentration for these three samples was calculated

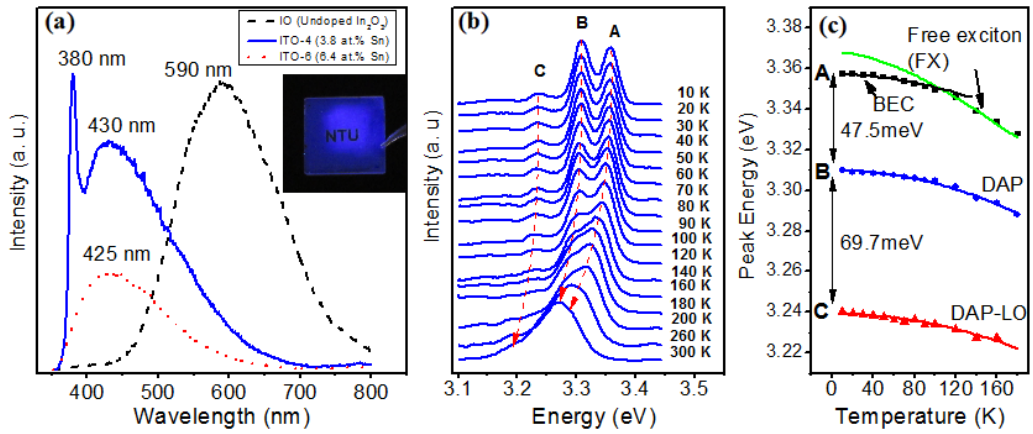

Figure 7. (a) Room temperature PL spectra taken on three typical samples IO, ITO-4, and ITO-6 with Sn doping levels of 0, 3.8, and 6.4 at.%, respectively. The inset shows the photograph of blue emission from ITO nanowires under the illumination of a UV light source. (b) Temperature-dependent PL spectra measured from 10 to 300 K on the nanowire sample ITO-4 which has a Sn doping level of 3.8 at.%. (c) Temperature dependence of the PL peak energies. The lines are guides to the eyes.

to be $2.4 \pm 0.5 \times 10^{19}$, $1.9 \pm 0.4 \times 10^{20}$ and $2.6 \pm 0.6 \times 10^{20}$ cm^{-3}, which is comparable to the typical values in ITO thin films [44, 52].

We also conducted the room temperature PL measurements on these samples, and the data are shown in figure 7(a). The undoped In_2O_3 nanowire sample exhibits a broad green emission at about 590 nm (2.10 eV). It is well known that bulk In_2O_3 has no light emission at room temperature [53] while emission in the visible and UV range has been reported for nanomaterials [54–57], where its origin is generally attributed to deep level defects [58], such as surface defects and singly ionized oxygen vacancies (V_0^+) [59, 60]. Since surface defects exist abundantly in oxide nanowires due to their large surface-to-volume ratio and the VLS growth often gives rise to oxygen vacancies, it is not surprising that an intense visible light emission was observed in the In_2O_3 nanowires. It is interesting to note that the Sn doping shifts this visible emission to the higher energies, i.e. 430 nm (2.88 eV) and 425 nm (2.92 eV) in ITO-4 and ITO-6, respectively. Consequently, the ITO nanowire samples exhibit a blue color under the stimulation of a UV light source (see photograph in the inset of figure 7(a)). This emission can be ascribed to a new defect level introduced into the band gap by the Sn doping [61]. Electrons from this donor level recombine with photon-excited holes in the valence band, giving rise to the visible emission at ~2.9 eV.

More significantly, we observed a strong peak at 380 nm (3.263 eV) with a narrow FWHM = 10 nm in the UV region in the sample ITO-4 doped with 3.8 at.% Sn. Such a UV emission has not been reported in any ITO materials. This emission can be ascribed to the near band edge transition wherein photogenerated holes near the valence band recombine with electrons in the donor levels through a radiative process [54, 62, 55]. Such an efficient radiative process is often associated with a high crystalline quality or some quantum confinement effects [54]. Since the quantum confinement effect should be quite weak given the size of the ITO nanowires (~180 nm), the appearance of this UV emission underscores the high quality of the as-synthesized ITO nanowires. Interestingly, this UV emission disappears in the sample ITO-6 with a higher Sn doping, leaving only a broad peak in the visible range, which indicates that the high crystalline quality is lost due to the doping induced structural disorder.

To gain an insight into the detailed emission mechanism, temperature-dependent PL measurements from 10 to 300 K were carried out on the sample ITO-4 with 3.8 at.% Sn doping. As shown in figure 7(b), three distinct peaks were observed at low temperatures (e.g. $T = 10$ K), and such radiative fine structures, to our knowledge, have not been reported in any ITO material so far. We can understand their excitonic origin by comparing them with the UV emissions in other wide band gap oxides such as ZnO and SnO_2 [63–68]. The strongest peak near 3.310 eV (peak B) can be attributed to the donor–acceptor pair (DAP) transition while the weakest peak (peak C) at 3.240 eV is its first order longitudinal optical (LO)-phonon replica. The energy difference between the DAP emission and its first order phonon replica is 69.7 meV, which is maintained for the whole temperature range, and notably this energy is close to the phonon energy in In_2O_3 [48]. The coupling strength between the radiative transition and the LO-phonon is characterized by the Huang–Rhys factor S [69], which relates the relative intensity of the nth phonon replica I_n with the primary peak I_0:

$$I_n = I_0(S^n e^{-S}/n!), \qquad n = 1, 2, 3, \ldots. \tag{3}$$

From the PL spectra, the S factor associated with DAP was estimated to be 0.2.

The temperature-dependent evolution of the peak energies is summarized in figure 7(c). Red shifts were observed for all three peaks as the measurement temperature increases, which can be ascribed to the narrowing of the band gap [70, 71]. Peak A near 3.358 eV can be ascribed to the radiative combination of bound exciton complexes (BECs) [63, 72]. This bound exciton emission weakens as temperature increases and completely disappears at high temperatures due to the thermal ionization. It is followed by the free exciton emission (FX) which

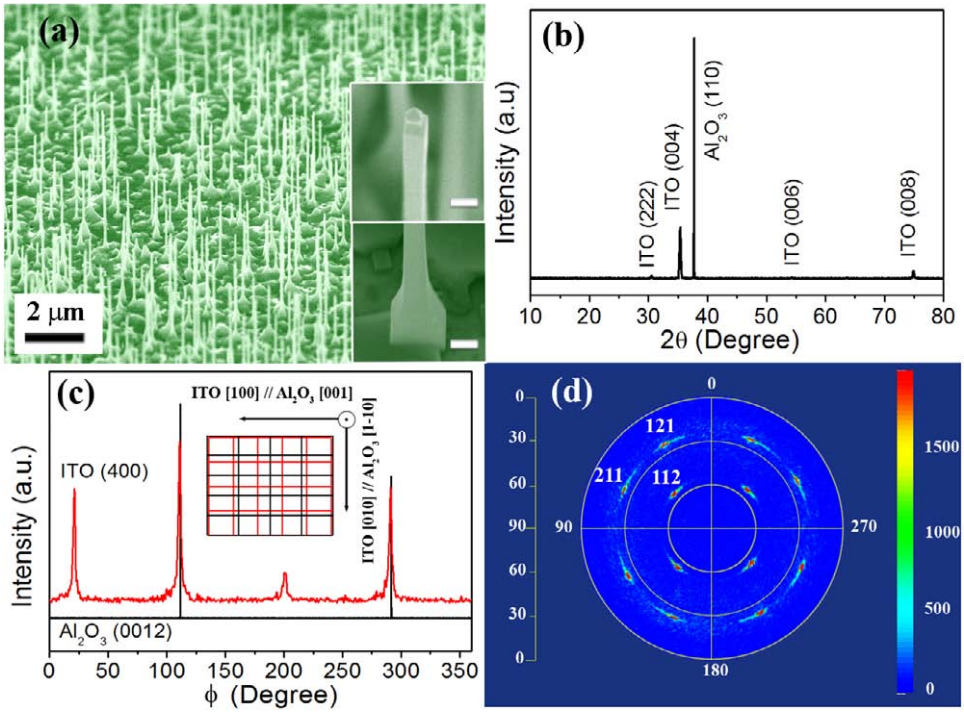

Figure 8. (a) SEM perspective view of the vertically aligned ITO nanowire arrays grown on the α-plane sapphire substrate. Insets are the enlarged view of the top (upper) and bottom (lower) of an ITO nanowire. Scale bars in the insets correspond to 100 nm. (b) XRD two-theta scan on the aligned ITO nanowire sample. (c) XRD in-plane phi scans of ITO (400) and Al_2O_3 (0012) planes. Inset is a schematic of the epitaxial relationship between ITO (001) (red grid) and α-sapphire (black grid). (d) XRD pole figure of the ITO {211} planes.

dominates at temperatures higher than 100 K [63, 65]. The temperature dependence of the integrated DAP peak intensity was fitted with a phenomenological dual activation energy model (supporting information available at stacks.iop.org/Nano/22/195706/mmedia) [73], and the activation energies were estimated to be 11 and 132 meV, which can be ascribed as the binding energies of donors and acceptors, respectively [65]. The shallow donor and acceptor levels contributing to the prominent DAP emission may originate from neutral oxygen vacancies and indium–oxygen vacancy centers [74, 75]. However, to understand the underlying mechanism of the activation process in ITO nanowires entails further investigations.

3.4. Growth of aligned ITO nanowires

Considering that aligned nanowires are important for many electrical and optical applications, we achieved the growth of vertically aligned ITO nanowires on α-plane sapphire substrates. This epitaxial growth of ITO nanowires on sapphire has not been demonstrated before. Figure 8(a) shows a perspective SEM image of the vertically aligned ITO nanowire arrays. The catalyst nanoparticles on the top of nanowires suggest the same VLS growth mechanism as the randomly aligned nanowires, and the nanowires grow from the square-shaped tapering pedestals underneath (see insets of figure 8(a)).

To determine the epitaxial relationship between ITO nanowires and sapphire substrate, we carried out detailed structural characterizations. Figure 8(b) is the XRD 2-theta scan on the aligned nanowire sample, showing the dominant ITO (00k) diffraction peaks. It also suggests an epitaxial growth direction of ITO (001) aligning with the sapphire (110). Figure 8(c) gives a phi scan of the ITO (400) planes of the nanowires which shows a four-fold symmetry owing to the cubic crystal structure of ITO. The average FWHM of the diffraction peaks is 2.5°, indicating a good in-plane orientation of the aligned ITO nanowires. Its comparison with the sapphire phi scan suggests an in-plane epitaxial relationship of ITO [100] ∥ Al_2O_3 [001] and ITO [010] ∥ Al_2O_3 [1$\bar{1}$0] (inset of figure 8(c)), and the lattice mismatches along these two directions are 2.6 and 2.3%, respectively. This good epitaxial growth of ITO nanowires on α-cut sapphire substrates is further evidenced in the pole figure taken for the ITO {211} plane, as shown in figure 8(d). We observed three distinct sets of four-fold symmetric diffraction peaks corresponding to the {112}, {121}, and {211} families located at tilting angles of 55°, 25°, and 25°, respectively. Thus, these aligned ITO nanowires open doors for further optical investigations, and may facilitate the construction of electronic and photonic nanodevices.

4. Conclusions

In summary, high quality ITO nanowires with Sn doping level tuned from 1.0 to 6.4 at.% were synthesized via the physical vapor transport method. A Sn doping concentration of up to 6.4 at.% was achieved at a growth temperature of 840 °C, which suggests that our synthesis route is a more efficient doping method than the conventional solid state reaction. As a promising multifunctional nanomaterial, these

ITO nanowires are not only conducting, i.e. a sheet resistance of as low as 6.4 Ω/□ for nanowire layers and a resistivity of 2.4×10^{-4} Ω cm for individual nanowires, and transparent, i.e. a high transmittance in both the visible (∼80%) and near infrared (>90%) range, but also exhibit for the first time a room temperature excitonic UV emission. Moreover, we demonstrated the first epitaxial synthesis of vertically aligned ITO nanowires on α-sapphire substrates which may facilitates future device applications. Our results on these bottom-up synthesized single crystalline ITO nanowires with tunable doping and promising physical properties encourage the future integration of these light emitting TCO nanomaterials into functional electronic and optoelectronics devices.

Acknowledgment

We thank the Singapore National Research Foundation for support.

References

[1] Ngamsinlapasathian S, Sreethawong T, Suzuki Y and Yoshikawa S 2006 Doubled layered ITO/SnO_2 conducting glass for substrate of dye-sensitized solar cells *Sol. Energy Mater. Sol. Cells* **90** 2129–40

[2] Hyam R S, Bhosale R K, Lee W, Han S H, Hannoyer B and Ogale S B 2010 Room temperature synthesis of rutile TiO_2 hierarchical nanoneedle flower morphology for dye sensitized solar cell *J. Nanosci. Nanotechnol.* **10** 5894–8

[3] El Hichou A, Addou M, Mansori M and Ebothé J 2009 Structural, optical and luminescent characteristics of sprayed fluorine-doped In_2O_3 thin films for solar cells *Sol. Energy Mater. Sol. Cells* **93** 609–12

[4] Wan Q, Dattoli E, Fung W, Guo W, Chen Y, Pan X and Lu W 2006 High-performance transparent conducting oxide nanowires *Nano Lett.* **6** 2909–15

[5] Kim H, Horwitz J S, Ianno N J, Woollam J A, Kafafi Z H and Chrisey D B 2002 Highly oriented indium tin oxide films for high efficiency organic light emitting diodes *J. Appl. Phys.* **91** 5371–6

[6] Yan J, Fang X S, Zhang L D, Bando Y, Gautam U K, Dierre B, Sekiguchi T and Golberg D 2008 Structure and cathodoluminescence of individual ZnS/ZnO biaxial nanobelt heterostructures *Nano Lett.* **8** 2794–9

[7] Zhang Z, Gao J, Wong L, Tao J, Liao L, Zheng Z, Xing G, Peng H, Yu T and Shen Z 2009 Morphology-controlled synthesis and a comparative study of the physical properties of SnO_2 nanostructures: from ultrathin nanowires to ultrawide nanobelts *Nanotechnology* **20** 135605

[8] McAlpine M, Friedman R, Jin S, Lin K, Wang W and Lieber C 2003 High-performance nanowire electronics and photonics on glass and plastic substrates *Nano Lett.* **3** 1531–5

[9] Sun Y G and Rogers J A 2007 Inorganic semiconductors for flexible electronics *Adv. Mater.* **19** 1897–916

[10] Zhang D H, Ryu K, Liu X L, Polikarpov E, Ly J, Tompson M E and Zhou C W 2006 Transparent, conductive, and flexible carbon nanotube films and their application in organic light-emitting diodes *Nano Lett.* **6** 1880–6

[11] Lee J Y, Connor S T, Cui Y and Peumans P 2008 Solution-processed metal nanowire mesh transparent electrodes *Nano Lett.* **8** 689–92

[12] O'Dwyer C, Szachowicz M, Visimberga G, Lavayen V, Newcomb S and Torres C 2009 Bottom–up growth of fully transparent contact layers of indium tin oxide nanowires for light-emitting devices *Nat. Nanotechnol.* **4** 239–44

[13] Wan Q, Wei M, Zhi D, MacManus-Driscoll J and Blamire M 2006 Epitaxial growth of vertically aligned and branched single-crystalline tin-doped indium oxide nanowire arrays *Adv. Mater.* **18** 234–8

[14] Nguyen P, Ng H T, Kong J, Cassell A M, Quinn R, Li J, Han J, McNeil M and Meyyappan M 2003 Epitaxial directional growth of indium-doped tin oxide nanowire arrays *Nano Lett.* **3** 925–8

[15] Zhang Z, Wong L M, Ong H G, Wang X J, Wang J L, Wang S J, Chen H Y and Wu T 2008 Self-assembled shape- and orientation-controlled synthesis of nanoscale Cu_3Si triangles, squares, and wires *Nano Lett.* **8** 3205–10

[16] Wang D, Xing G, Peng H and Wu T 2009 Chlorine-assisted size-controlled synthesis and tunable photoluminescence in Cr-doped silica nanospheres *J. Phys. Chem.* C **113** 7065–8

[17] Xing G Z, Yi J B, Wang D D, Liao L, Yu T, Shen Z X, Huan C H A, Sum T C, Ding J and Wu T 2009 Strong correlation between ferromagnetism and oxygen deficiency in Cr-doped In_2O_3 nanostructures *Phys. Rev.* B **79** 174406

[18] Zhang Z, Wong L M, Wang H X, Wei Z P, Zhou W, Wang S J and Wu T 2010 Self-assembled in-plane growth of Mg_2SiO_4 nanowires on Si substrates catalyzed by Au nanoparticles *Adv. Funct. Mater.* **20** 2511–8

[19] Guo D L, Huang X, Xing G Z, Zhang Z, Li G P, He M, Zhang H, Chen H and Wu T 2011 Metal-layer-assisted coalescence of Au nanoparticles and its effect on diameter control in vapor–liquid–solid growth of oxide nanowires *Phys. Rev.* B **83** 045403

[20] van der Pauw L J 1958 A method of measuring specific resistivity and hall effect of discs of arbitrary shape *Phil. Res. Rep.* **13** 1–9

[21] Wagner R S, Ellis W C, Jackson K A and Arnold S M 1964 Study of the filamentary growth of silicon crystal from the vapor *J. Appl. Phys.* **55** 2993–3000

[22] Wagner R S and Ellis W C 1964 Vapor–liquid–solid mechanism of single crystal growth *Appl. Phys. Lett.* **4** 89–90

[23] Zhang Z, Wang S J, Yu T and Wu T 2007 Controlling the growth mechanism of ZnO nanowires by selecting catalysts *J. Phys. Chem.* C **111** 17500–5

[24] Gonzalez G B, Cohen J B, Hwang J H, Mason T O, Hodges J P and Jorgensen J D 2001 Neutron diffraction study on the defect structure of indium–tin–oxide *J. Appl. Phys.* **89** 2550–5

[25] Neri G, Bonavita A, Micali G, Rizzo G, Pinna N, Niederberger M and Ba J 2007 A study on the microstructure and gas sensing properties of ITO nanocrystals *Thin Solid Films* **515** 8637–40

[26] Frank G and Kostlin H 1982 Electrical-properties and defect model of tin-doped indium oxide layers *Appl. Phys.* A **27** 197–206

[27] Frank G, Kostlin H and Rabenau A 1979 X-ray and optical measurement in the In_2O_3–SnO_2 system *Phys. Status Solidi* a **52** 231–8

[28] Nadaud N, Lequeux N, Nanot M, Jove J and Roisnel T 1998 Structural studies of tin-doped indium oxide (ITO) and $In_4Sn_3O_{12}$ *J. Solid State Chem.* **135** 140–8

[29] Udawatte C, Yanagisawa K and Nasu S 2000 Sintering of additive free hydrothermally derived indium tin oxide powders in air *J. Solid State Chem.* **154** 444–50

[30] Heward W and Swenson D 2007 Phase equilibria in the pseudo-binary In_2O_3–SnO_2 system *J. Mater. Sci.* **42** 7135–40

[31] Dean J A 1992 *Lange's Handbook of Chemistry* (New York: McGraw-Hill)

[32] Szuber J, Czempik G, Larciprete R, Koziej D and Adamowicz B 2001 XPS study of the L-CVD deposited SnO_2 thin films exposed to oxygen and hydrogen *Thin Solid Films* **391** 198–203

[33] Dalpian G and Chelikowsky J 2006 Self-purification in semiconductor nanocrystals *Phys. Rev. Lett.* **96** 226802

[34] Erwin S C, Zu L J, Haftel M I, Efros A L, Kennedy T A and Norris D J 2005 Doping semiconductor nanocrystals *Nature* **436** 91–4

[35] Okamoto H and Massalski T B 1990 *Binary Alloy Phase Diagrams* ed T B Massalski *et al* (Materials Park, OH: ASM International)

[36] Morales E H, He Y B, Vinnichenko M, Delley B and Diebold U 2008 Surface structure of Sn-doped In_2O_3 (111) thin films by STM *New J. Phys.* **10** 125030

[37] Morales E H and Diebold U 2009 The structure of the polar Sn-doped indium oxide (001) surface *Appl. Phys. Lett.* **95** 253105

[38] Prasad R, Singh M P, Prellier W, Siwach P K, Rawat R, Kaur A and Singh H K 2009 Comparative study of transport properties of compressively strained epitaxial and polycrystalline $La_{0.88}Sr_{0.12}MnO_3$ thin films *Phys. Status Solidi* b **246** 1662–73

[39] Minami T 2005 Transparent conducting oxide semiconductors for transparent electrodes *Semicond. Sci. Technol.* **20** S35

[40] Kim H and Gilmore C M 1999 Electrical, optical, and structural properties of indium–tin–oxide thin films for organic light-emitting devices *J. Appl. Phys.* **86** 6451–61

[41] Noguchi S and Sakata H 1981 Electrical properties of Sn doped In_2O_3 films prepared by reactive evaporation *J. Phys. D: Appl. Phys.* **14** 2631

[42] Mizuhashi M 1980 Electrical-properties of vaccum-deposited indium oxide and indium tin oxide films *Thin Solid Films* **70** 91–100

[43] Manifacier J C 1982 Thin metallic oxides as transparent conductors *Thin Solid Films* **90** 297–308

[44] Agnihotry S A, Saini K K, Saxena T K, Nagpal K C and Chandra S 1985 Studies on e-beam deposited transparent conductive films of In_2O_3–Sn at moderate substrate temperatures *J. Phys. D: Appl. Phys.* **18** 2087–96

[45] Munir M M, Widiyandari H, Iskandar F and Okuyama K 2008 Patterned indium tin oxide nanofiber films and their electrical and optical performance *Nanotechnology* **19** 375601

[46] Walsh A, Da Silva J L F, Wei S H, Korber C, Klein A, Piper L F J, DeMasi A, Smith K E, Panaccione G, Torelli P, Payne D J, Bourlange A and Egdell R G 2008 Nature of the band gap of In_2O_3 revealed by first-principles calculations and x-ray spectroscopy *Phys. Rev. Lett.* **100** 167402

[47] Tauc J, Grigorovici R and Vancu A 1966 Optical properties and electronic structure of amorphous germanium *Phys. Status Solidi* **15** 627–37

[48] Weiher R L and Ley R P 1966 Optical properties of indium oxide *J. Appl. Phys.* **37** 299–302

[49] Burstein E 1954 Anomalous optical absorption limit in InSb *Phys. Rev.* **93** 632–3

[50] Hamberg I and Granqvist C G 1986 Evaporated Sn-doped In_2O_3 films-basic optical properties and applications to energy efficient windows *J. Appl. Phys.* **60** R123–59

[51] Dixit A, Sudakar C, Naik R, Naik V M and Lawes G 2009 Undoped vacuum annealed In_2O_3 thin films as a transparent conducting oxide *Appl. Phys. Lett.* **95** 192105

[52] Coutal C, Azema A and Roustan J C 1996 Fabrication and characterization of ITO thin films deposited by excimer laser evaporation *Thin Solid Films* **288** 248–53

[53] Ohhata Y, Shinoki F and Yoshida S 1979 Optical properties of r.f. reactive sputtered tin-doped In_2O_3 films *Thin Solid Films* **59** 255–61

[54] Cao H, Qiu X, Liang Y and Zhu Q 2003 Room temperature ultraviolet-emitting In_2O_3 nanowires *Appl. Phys. Lett.* **83** 761–3

[55] Chen C-J, Xu W-L and Chern M-Y 2007 Low-temperature epitaxial growth of vertical In_2O_3 nanowires on A-plane sapphire with hexagonal cross-section *Adv. Mater.* **19** 3012–5

[56] Zeng F, Zhang X, Wang J, Wang L and Zhang L 2004 Large-scale growth of In_2O_3 nanowires and their optical properties *Nanotechnology* **15** 596–600

[57] Liang C, Meng G, Lei Y, Phillipp F and Zhang L 2001 Catalytic growth of semiconducting In_2O_3 nanofibers *Adv. Mater.* **13** 1330–3

[58] Hsin C L, He J H and Chen L J 2006 Modulation of photoemission spectra of In_2O_3 nanowires by the variation in Zn doping level *Appl. Phys. Lett.* **88** 063111

[59] Li Y, Bando Y and Golberg D 2003 Single-crystalline In_2O_3 nanotubes filled with In *Adv. Mater.* **15** 581–5

[60] Peng X S, Meng G W, Zhang J, Wang X F, Wang Y W, Wang C Z and Zhang L D 2002 Synthesis and photoluminescence of single-crystalline In_2O_3 nanowires *J. Mater. Chem.* **12** 1602–5

[61] Cao Y A, Yang W S, Zhang W F, Liu G Z and Yue P L 2004 Improved photocatalytic activity of Sn^{4+} doped TiO_2 nanoparticulate films prepared by plasma-enhanced chemical vapor deposition *New J. Chem.* **28** 218–22

[62] Wei Z P, Guo D L, Liu B, Chen R, Wong L M, Yang W F, Wang S J, Sun H D and Wu T 2010 Ultraviolet light emission and excitonic fine structures in ultrathin single-crystalline indium oxide nanowires *Appl. Phys. Lett.* **96** 031902

[63] Hur T-B, Jeen G S, Hwang Y-H and Kim H-K 2003 Photoluminescence of polycrystalline ZnO under different annealing conditions *J. Appl. Phys.* **94** 5787–90

[64] Jie J, Wang G, Chen Y, Han X, Wang Q and Xu B 2005 Synthesis and optical properties of well-aligned ZnO nanorod array on an undoped ZnO film *Appl. Phys. Lett.* **86** 031909

[65] Chen R, Xing G Z, Gao J, Zhang Z, Wu T and Sun H D 2009 Characteristics of ultraviolet photoluminescence from high quality tin oxide nanowires *Appl. Phys. Lett.* **95** 061908

[66] Blattner G, Klingshirn C and Helbig R 1980 Impurity transitions in the photo-luminescence spectra of SnO_2 *Solid State Commun.* **33** 341–4

[67] Ghosh R, Basak D and Fujihara S 2004 Effect of substrate-induced strain on the structural, electrical, and optical properties of polycrystalline ZnO thin films *J. Appl. Phys.* **96** 2689–92

[68] Antony J, Chen X, Morrison J, Bergman L, Qiang Y, McCready D and Engelhard M 2005 ZnO nanoclusters: Synthesis and photoluminescence *Appl. Phys. Lett.* **87** 241917

[69] Toyozawa Y and Hermanso J 1968 Exciton-phonon bound state—a new quasiparticle *Phys. Rev. Lett.* **21** 1637–41

[70] Kar A, Stroscio M A, Dutta M, Kumari J and Meyyappan M 2009 Observation of ultraviolet emission and effect of surface states on the luminescence from tin oxide nanowires *Appl. Phys. Lett.* **94** 101905

[71] Varshni Y P 1967 Temperature dependence of energy gap in semiconductors *Physica* **34** 149–54

[72] Zhang B P, Binh N T, Segawa Y, Wakatsuki K and Usami N 2003 Optical properties of ZnO rods formed by metalorganic chemical vapor deposition *Appl. Phys. Lett.* **83** 1635–7

[73] Sun H D, Calvez S, Dawson M D, Gupta J A, Aers G C and Sproule G I 2006 Thermal quenching mechanism of photoluminescence in 1.55 μm GaInNAsSb/Ga(N)As quantum-well structures *Appl. Phys. Lett.* **89** 101909

[74] Wu X C, Hong J M, Han Z J and Tao Y R 2003 Fabrication and photoluminescence characteristics of single crystalline In_2O_3 nanowires *Chem. Phys. Lett.* **373** 28–32

[75] Kar A, Stroscio M A, Dutta M, Kumari J and Meyyappan M 2010 Growth and properties of tin oxide nanowires and the effect of annealing conditions *Semicond. Sci. Technol.* **25** 024012